Dielectric screening at TMD:hBN interfaces: Monolayer-to-bulk transition, local-field effect, and spatial dependence

Olugbenga Adeniran and Zhen-Fei Liu*
Department of Chemistry, Wayne State University, Detroit, Michigan 48202, USA

(Received 3 December 2022; revised 6 April 2023; accepted 18 April 2023; published 4 May 2023)

The dielectric effects of a substrate have been shown to be important for modulating the electronic properties of an adsorbate, especially in van der Waals heterostructures. Here, using the first-principles dielectric embedding *GW* approach within the framework of many-body perturbation theory, we perform a case study on the dielectric screening effects of hexagonal boron nitride (hBN) on various transition-metal dichalcogenides (TMDs). We consider three systems, monolayer MoS_2, bilayer MoS_2, and a mixed WS_2/MoS_2 bilayer adsorbed on hBN, and examine three aspects of the substrate dielectric screening: (i) the thickness dependence and the monolayer-to-bulk transition, for which we consider the effects of one-, two-, three-, and four-layer hBN; (ii) the local-field effect, for which we numerically assess a common approximation of neglecting the in-plane local-field components of the substrate polarizability; and (iii) the spatial dependence, for which we consider the mixed WS_2/MoS_2 bilayer adsorbed on hBN with either side facing the substrate. Our results provide quantitative insight into how the substrate screening effects can be leveraged for band structure engineering.

DOI: 10.1103/PhysRevMaterials.7.054001

I. INTRODUCTION

Transition-metal dichalcogenides (TMDs) such as MoS_2 and WS_2 exhibit unique electronic and optical properties due to quantum confinement as a result of their low dimensionality [1–4]. Experimentally, such two-dimensional (2D) materials are often fabricated on substrates via chemical vapor deposition [5,6]. TMD-based devices, such as field-effect transistors [7–9], are often operated with the support of a substrate, too. The coupling between the TMD adsorbates and the supporting substrates is usually van der Waals interaction, indicating little orbital hybridization. However, due to the long-range nature of the Coulomb interaction, it has been extensively shown that the substrates act as dielectric media and effectively screen the Coulomb interaction within the adsorbate [10–13], resulting in renormalizations in the fundamental (transport) band gaps and optical excitation energies of the adsorbate [14–16].

For TMDs, commonly used substrates include Au [17–19], graphene/graphite [20–23], SiO_2/Si [24–26], and hexagonal boron nitride (hBN) [5,27,28]. Since large-gap insulators are generally believed to have low dielectric constants [29], one might naively assume that SiO_2 and hBN (both having band gaps over 6 eV) do not significantly alter the electronic and optical properties of the materials adsorbed on them. However, this has been shown to be not the case. For instance, Ref. [30] showed that both SiO_2 and hBN substrates could considerably modulate the local electronic structure and optical properties of monolayer MoS_2.

Due to the wide use of substrates, it is somewhat challenging to extract the properties of a "freestanding" TMD monolayer in experiments and quantify the effects of the substrates. For this purpose, first-principles calculations play an indispensable role. It is now common knowledge that one needs many-body perturbation theory to accurately describe the quasiparticle and excitonic properties of 2D materials due to deficiencies in typical functionals [31–33] within the framework of density functional theory (DFT). The first-principles *GW* and Bethe-Salpeter equation [34–37] (G, Green's function; W, screened Coulomb interaction) have been shown to be essential in quantitative descriptions of the quasiparticle and optical properties of pristine TMDs [38–41], in which local and semilocal functionals in the DFT framework significantly underestimate the band gaps of 2D materials. As far as their interfaces with substrates are concerned, due to the presence of supercells, various approximations have been made to keep the computational cost at a manageable level. Among others, the substrate screening approximation [42] captures the dielectric screening from the substrate [43,44] and has proven to be successful for weakly coupled (without significant orbital hybridization) interfaces [45–47]. Within the framework of substrate screening, additional approximations are often made to further reduce the computational cost, including the neglect of the local-field components in the noninteracting polarizability or response function χ^0 of the substrate along directions parallel to the surface [42] and the use of model dielectric functions for the substrate [16,48]. However, the numerical consequences of such additional approximations have not been fully examined, which we address in this work.

In this work, we quantitatively study the effect of a hBN substrate on three adsorbates: monolayer MoS_2, bilayer MoS_2, and the WS_2/MoS_2 bilayer heterostructure. To focus on the dielectric effect of the substrate on modulating the electronic structure of the adsorbates, we employ the dielectric embedding *GW* approach [49], which yields quantitative agreement with direct *GW* calculations of the interface, as

*zfliu@wayne.edu

we explicitly show below. Using monolayer MoS_2 adsorbed on few-layer hBN as an example, we first illustrate how the dielectric effect of the substrate grows with the thickness of the hBN and conclude that it converges at four layers. Then we numerically assess a commonly used approximation, namely, the neglect of the local-field components in $\chi^0_{\rm hBN}$ along directions parallel to the surface. After that, we study bilayer MoS_2 adsorbed on four-layer hBN and show how the substrate lifts the degeneracy of the bilayer MoS_2 bands. Last, we study the WS_2/MoS_2 bilayer adsorbed on four-layer hBN and furthermore compare two scenarios in which either the MoS_2 or WS_2 side faces the hBN substrate upon adsorption. We demonstrate that the substrate screening is spatially dependent and can be leveraged to selectively modulate certain bands of the WS_2/MoS_2 bilayer.

This paper is structured as follows. In Sec. II, we describe the computational details and report parameters adopted in our calculations. In Sec. III, the main results are presented: the thickness-dependent dielectric screening of hBN in the context of monolayer MoS_2 adsorbed on few-layer hBN (Sec. III A), the numerical assessment of the in-plane local-field effects of $\chi^0_{\rm hBN}$ (Sec. III B), the case of bilayer MoS_2 adsorbed on four-layer hBN and the related degeneracy lifting (Sec. III C), and the WS_2/MoS_2 bilayer adsorbed on four-layer hBN (Sec. III D), which includes a discussion of the spatial dependence of the substrate dielectric effect. We make concluding remarks in Sec. IV.

II. COMPUTATIONAL DETAILS

We adopt the lattice parameters and atomic coordinates of a monolayer MoS_2 unit cell from our previous work [50], where the in-plane lattice parameter is 3.15 Å, relaxed using the vdw-DF-cx functional (van der Waals density functional with consistent exchange) [51]. To explicitly assess the in-plane local-field effect of $\chi^0_{\rm hBN}$, we need to construct a commensurate supercell for the interface formed between MoS_2 and hBN. To minimize the strain on hBN, we construct a supercell containing 4×4 MoS_2 unit cells and 5×5 hBN unit cells. The resulting hBN in-plane lattice parameter is 2.52 Å, corresponding to a 0.8% expansive strain compared to the experimental lattice parameter of 2.50 Å [52]. The internal coordinates of hBN are relaxed using the vdw-DF-cx functional. We have checked that the band structure of hBN is not qualitatively affected by this strain. The length of the unit cell along the out-of-plane direction is 45 Å, allowing for sufficient vacuum. Multilayer hBN systems are modeled by placing additional hBN layer(s) 3.3 Å apart from one another, consistent with Ref. [53] and experiment [52]. For bilayer MoS_2 and heterobilayer WS_2/MoS_2, we adopt the AA′ stacking and fully relax the atomic coordinates using the vdw-DF-cx functional until all residual forces are below 0.05 eV/Å. We optimize the adsorption height of each adsorbate on the hBN substrate using the vdw-DF-cx functional without further relaxation of the internal atomic coordinates of the adsorbate or substrate, resulting in an approximately 3.3 Å adsorption height for each interface. All DFT calculations employ the optimized norm-conserving Vanderbilt pseudopotentials [54,55] and the QUANTUM ESPRESSO package [56]. Figure 1 shows all systems studied in this work.

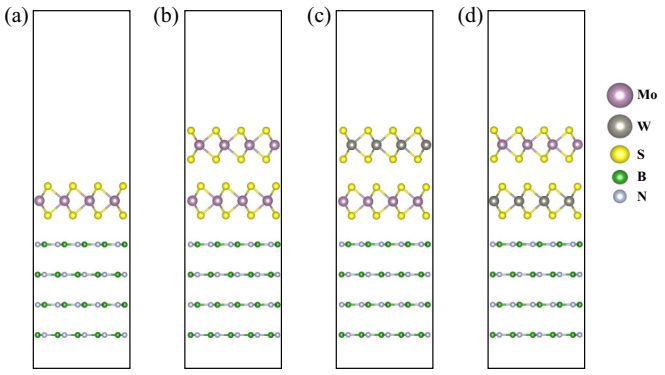

FIG. 1. The side views of the systems studied in this work. (a) Monolayer MoS_2 adsorbed on four-layer hBN (interfaces with one-, two-, and three-layer hBN are not shown). (b) Bilayer MoS_2 adsorbed on four-layer hBN. (c) WS_2/MoS_2 bilayer adsorbed on hBN, with MoS_2 being closer to the substrate. (d) WS_2/MoS_2 bilayer adsorbed on hBN, with WS_2 being closer to the substrate. The black boxes represent periodic boundary conditions. The amount of vacuum is not shown in scale. This figure was rendered using VESTA [57].

For the *GW* calculations, we employ the dielectric embedding *GW* scheme [49] to focus on the dielectric effects of the hBN substrate on the TMD adsorbates. Using MoS_2 adsorbed on monolayer hBN as an example, we have checked explicitly that the results from the dielectric embedding *GW* agree well with those obtained from a direct *GW* calculation of the MoS_2:hBN interface system. In the dielectric embedding *GW* approach, the dielectric function is determined from a combined χ^0, i.e., $\chi^0(\mathbf{q}) = \chi^0_{\rm TMD}(\mathbf{q}) + \chi^0_{\rm hBN}(\mathbf{q})$. Physically, this approximation of χ^0 neglects the orbital hybridization or mixing between TMD and hBN, which is a good approximation given the fact that the interaction between the two materials is mainly van der Waals. Both $\chi^0_{\rm TMD}$ and $\chi^0_{\rm hBN}$ are first calculated in their corresponding unit cells and then folded in the reciprocal space into the interface supercells. For both subsystems, we use a 5 Ry dielectric cutoff and 200 bands in the summation to compute χ^0 and 30 bands on a shifted $\mathbf{k}$ grid for the treatment of the $\mathbf{q}\to0$ limit. A $\mathbf{q}$ mesh of $20\times20\times1$ ($25\times25\times1$) is used for the TMD (hBN) unit cell. The resulting combined χ^0 for the interface supercell is then expressed on a $\mathbf{q}$ mesh of $5\times5\times1$.

In the dielectric embedding *GW* approach, the self-energy calculations are performed for the supercells of TMD adsorbates in the original interface simulation cells without explicitly including the substrate atoms. Physically, this approach neglects the overlap of TMD and hBN orbitals in the expression for the self-energy [49], consistent with the approximation of χ^0 discussed above. The calculations use a $\mathbf{k}$ mesh of $5\times5\times1$, a 5 Ry dielectric cutoff, and 4800 bands in the summation for the Green's function. All *GW* calculations are at the G_0W_0 level as implemented in the BERKELEYGW package [58] using the Perdew-Burke-Ernzerhof (PBE) functional [59] as the mean-field starting point. The frequency dependence of the dielectric function is treated using the Hybertsen-Louie generalized plasmon-pole model [36], with the plasma frequency in the embedding *GW* calculation of the

TMD set to be that from the corresponding TMD:hBN interface [49]. The $\mathbf{q} \to 0$ limit is treated using the semiconductor screening, and the spurious long-range interactions along the out-of-plane direction are removed by employing the slab Coulomb truncation [60]. The static remainder [61] is used to improve the convergence of the self-energy. All *GW* band structures are obtained via interpolation of the quasiparticle corrections from the explicitly computed $5 \times 5 \times 1$ **k** mesh to uniformly sampled **k** points along the high-symmetry lines in the Brillouin zone, as implemented in the BERKELEYGW package [58].

III. RESULTS AND DISCUSSION

A. Monolayer MoS_2 on few-layer hBN

We first study how the dielectric screening effect of the hBN substrate varies as the number of hBN layers increases. This will provide insight into the difference between two common scenarios explored in experiments and modeling, i.e., a one-layer hBN substrate [62,63] versus a few-layer hBN substrate [5,30]. Furthermore, it will indicate the minimum number of hBN layers needed in computational modeling to mimic the dielectric effect of a semi-infinite hBN substrate on an adsorbate.

Figure 2 illustrates how the band gap [Figs. 2(a) and 2(b)], conduction band minimum (CBM) energies [Figs. 2(c) and 2(d)], and valence band maximum (VBM) energies [Figs. 2(e) and 2(f)] vary as a function of the number of hBN layers at two different **k** points in the Brillouin zone: Γ [Figs. 2(a), 2(c) and 2(e)] and (0.4,0.4,0.0) [Figs. 2(b), 2(d), and 2(f)], where the latter is expressed in fractional coordinates (measured with respect to the lattice basis vectors) in reciprocal space. The Brillouin zone and in-plane reciprocal-space lattice vectors are shown in the inset in Fig. 3(b), which applies to all systems in this work. Monolayer MoS_2 is a direct gap material [64] with the band gap at the *K* point, and the direct band gap remains at the *K* point when MoS_2 is deposited on the hBN substrate. We report information at a **k** point of (0.4,0.4,0.0) simply because it is closest to *K* among all the directly calculated **k** points using *GW* (such that a numerical interpolation is not needed for Fig. 2). In each panel, the circles represent results from dielectric embedding *GW* calculations of MoS_2 (including in-plane local-field effects of χ^0_{hBN}; see Sec. III B for further details), with the vacuum level set to zero. Green crosses represent results from a direct *GW* calculation of the monolayer MoS_2:monolayer hBN interface as a benchmark for our dielectric embedding *GW* calculations. One can see that the dielectric embedding *GW* agrees with direct *GW* calculations within 0.1 eV for individual energy levels and within 0.05 eV for the gap.

Figure 2 shows interesting trends as the thickness of the hBN substrate grows. We first notice that one-layer hBN barely provides any dielectric screening to the monolayer MoS_2 adsorbate, as the VBM, CBM, and gap values do not change considerably compared to those of the freestanding monolayer MoS_2. Physically, this can be attributed to the fact that one-layer hBN is atomically thin, such that the adsorbate cannot induce a strong density response perpendicular to the surface "within" the substrate that is responsible for the dielectric screening. This might explain why single-layer hBN can be used as a "spacer" that effectively decouples an adsorbate from a substrate (see, e.g., Ref. [65] for an example in experiment). The dielectric screening becomes stronger as the number of hBN layers increases and eventually saturates when the number of hBN layers reaches four. Therefore, we conclude that for the purpose of modeling a semi-infinite hBN substrate, four layers are enough to converge the results within 0.1 eV, as far as the band gap of the adsorbate is concerned. This conclusion is in line with Ref. [53], where the monolayer-to-bulk transition of hBN band structure was analyzed in detail.

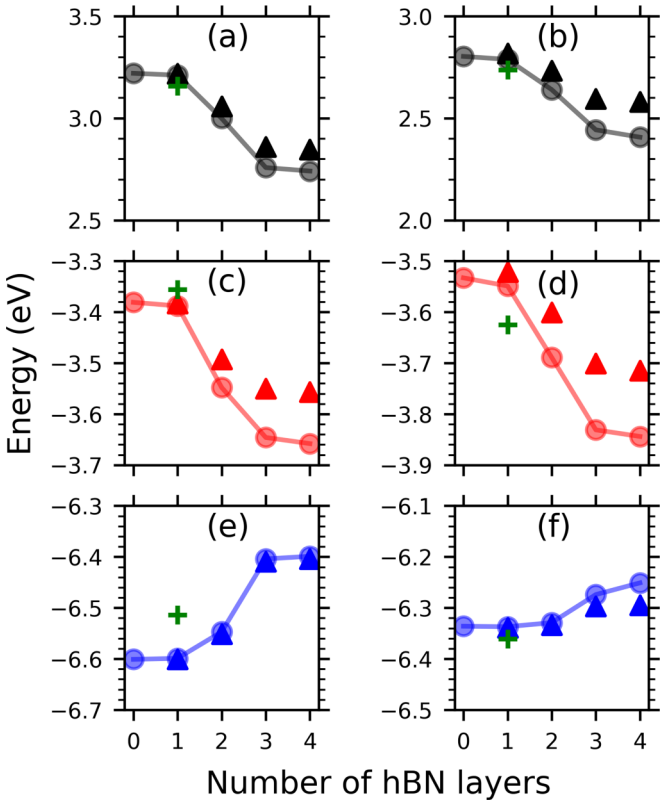

FIG. 2. Comparison of the band gap (black), the CBM energy (red), and the VBM energy (blue) at two different **k** points for monolayer MoS_2 adsorbed on few-layer hBN. Zero-layer hBN indicates a freestanding MoS_2 monolayer. All energies are measured with respect to the vacuum. (a), (c), and (e) are for the Γ point, while (b), (d), and (f) are for the **k** point with fractional coordinates (0.4,0.4,0.0), which is an explicitly computed **k** point closest to *K*, where the direct band gap of monolayer MoS_2 lies. Circles (triangles) represent results from the dielectric embedding *GW* calculations of MoS_2 with (without) the in-plane local-field effect of χ^0_{hBN}. Green crosses represent results from a direct *GW* calculation of an interface formed between monolayer MoS_2 and monolayer hBN.

It is worth mentioning that the dielectric embedding *GW* approach used here is particularly efficient for the purpose of studying the thickness dependence of the substrate dielectric screening. This is because we can bypass the calculation of the wave functions and dielectric functions of a series of large interfaces. Instead, we need to compute $\chi^0_{\mathrm{MoS_2}}$ only once and combine it with χ^0_{hBN} calculated for different layers of the

TABLE I. Comparison of different experimental and theoretical approaches that have been used to study the influence of the hBN substrate on the monolayer MoS_2 band gap (in eV). The MoS_2 gap listed for this work is the value at a **k** point of (0.4,0.4,0) [Fig. 2(b)], which should be numerically similar to the gap at the K point, given the small band curvature at K.

Method	Description of the hBN Dielectric Effect	MoS_2 Gap	Ref.
Sternheimer GW, Godby-Needs plasmon pole	Model W, $\epsilon_{\text{eff}} = (1+\epsilon_S)/2$, $\epsilon_S = 2.6$	2.58	[16]
Sternheimer GW, full frequency	Model W, $\epsilon_{\text{eff}} = (1+\epsilon_S)/2$, $\epsilon_S = 2.6$	2.50	[16]
Eigenvalue-self-consistent GW_0, full frequency	Similar to Eq. (3), extrapolated from a 14-layer hBN to semi-infinite thickness	2.36	[66]
LDA+GdW, $dW = W - W_{\text{metal}}$ [67]	Models for W and W_{metal}, $\epsilon_\infty^\parallel/\epsilon_\infty^\perp = 4.95/4.10$	2.73	[48]
LDA+G_0W_0	Monolayer hBN, similar to Eq. (3)	2.66	[68]
Scanning tunneling spectroscopy	Experiment	2.35	[30]
Dielectric embedding G_0W_0	Comparing Eqs. (2) and (3), four-layer hBN	2.41	This work

substrate, with both components explicitly calculated in their unit cells rather than supercells. Such a procedure can be easily generalized to analyze the effects of other substrates.

We compare our results to the existing literature. Table I compares prior experimental and theoretical studies of the dielectric screening effect of hBN on monolayer MoS_2. In particular, we list how each computational method treats the dielectric effect of the hBN substrate, either from first principles [66,68] or from model dielectric functions [16,48]. Our full first-principles GW results are consistent with other similar studies and experiments and provide another benchmark for developing model dielectric functions.

Last, we note in passing that we focus on the gap of monolayer MoS_2, rather than the band alignment between MoS_2 and hBN. DFT calculations indicate that the MoS_2:hBN interfaces are type I in the sense that the band edges of the MoS_2 are sandwiched between those of the hBN, and the VBM and CBM of the interfaces are entirely localized on MoS_2. While the VBM of the hBN substrate is within 1 eV (DFT result) below that of the MoS_2, the CBM of the hBN substrate is many eV above that of MoS_2. These energy level offsets are believed to be even larger in GW [16,48,66], such that the charge transfer between the two components is negligible.

B. In-plane local-field effect of substrate χ^0

Pioneered by Ref. [42], a common approximation in the study of the substrate dielectric effect is to neglect the in-plane (parallel to the surface) local-field components of the substrate χ^0, i.e.,

$$\bar{\chi}^0_{\text{hBN}}(\mathbf{G},\mathbf{G}';\mathbf{q}) = \chi^0_{\text{hBN}}(\mathbf{G},\mathbf{G}';\mathbf{q})\delta_{G_xG'_x}\delta_{G_yG'_y}, \tag{1}$$

where χ^0_{hBN} is the directly calculated χ^0 using the random-phase approximation and $\bar{\chi}^0$ neglects the in-plane local-field components of χ^0_{hBN}. Subsequently, in the substrate screening approximation,

$$\chi^0_{\text{tot}} \approx \chi^0_{\text{MoS}_2} + \chi^0_{\text{hBN}} \tag{2}$$

with the local-field effect, and

$$\bar{\chi}^0_{\text{tot}} \approx \chi^0_{\text{MoS}_2} + \bar{\chi}^0_{\text{hBN}} \tag{3}$$

without the local-field effect. Note that the local-field components of the adsorbate, i.e., those in $\chi^0_{\text{MoS}_2}$, are always included. The neglect of the substrate local-field effect enables calculations using incommensurate supercells between the adsorbate and the substrate [42] and greatly reduces the computational cost. However, to the best of our knowledge, its accuracy has not been explicitly examined. In this work, we assess the numerical consequence of Eq. (1) for the first time, in the context of monolayer MoS_2 adsorbed on few-layer hBN.

The results are shown in Fig. 2. Circles (triangles) represent results from Eq. (2) [Eq. (3)], i.e., with (without) the in-plane local-field components of χ^0_{hBN}. We can see that the local-field effect in the dielectric screening increases as the number of hBN layers increases. For the four-layer hBN substrate, the neglect of the local-field components in χ^0_{hBN} causes an error of 0.2 eV in the MoS_2 gap [Fig. 2(b)], which can be decomposed to a 0.15 eV error in the CBM [Fig. 2(d)] and another 0.05 eV error in the VBM [Fig. 2(f)]. Interestingly, we find that the local-field effect is larger at the (0.4,0.4,0.0) **k** point than at Γ and is larger for CBM than for VBM. This is likely due to the different shapes of the wave functions of the pertinent energy levels.

As a concluding remark, the neglect of local-field effects leads to a moderate error of 0.2 eV in the MoS_2 gap in the current study. However, the magnitude of the error may vary for other substrates or adsorbates. Therefore, we believe more systematic studies are needed to fully assess the numerical consequences of the local-field effects in the substrate dielectric screening.

C. Bilayer MoS_2 on four-layer hBN

Having established that the dielectric screening effect of the hBN substrate converges at four layers, we consider only TMDs adsorbed on four-layer hBN in subsequent calculations.

Figures 3(b) and 3(c) compare the GW band structure of the freestanding bilayer MoS_2 and that when it is adsorbed on four-layer hBN, where the latter is computed using the dielectric embedding GW approach. For the freestanding bilayer, we obtain a value of 2.0 eV for the quasiparticle gap, which is in good agreement with other GW calculations (1.9 eV from Ref. [41]). For MoS_2 adsorbed on four-layer hBN, the gap is reduced to 1.8 eV. Here, the gap renormalization of 0.2 eV is smaller than that of monolayer MoS_2 [0.4 eV; see Fig. 2(b)]. This is because, in bilayer MoS_2, the orbitals are delocalized over both layers, with electron distribution moving farther away from the substrate than in the case of monolayer MoS_2, resulting in weaker substrate dielectric screening.

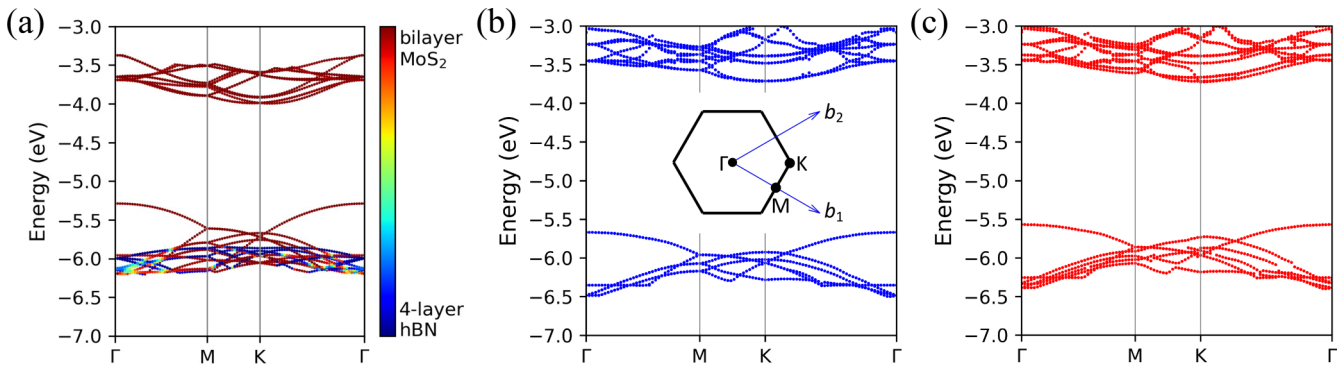

FIG. 3. (a) Color-coded PBE band structure of the bilayer MoS_2 adsorbed on four-layer hBN. (b) *GW* band structure of freestanding bilayer MoS_2. The inset shows the Brillouin zone and the high-symmetry points, as well as the in-plane reciprocal-space lattice vectors $\vec{b}_1$ and $\vec{b}_2$. (c) Band structure from a dielectric embedding *GW* calculation of bilayer MoS_2 adsorbed on four-layer hBN. All calculations are carried out in a 4×4 supercell of bilayer MoS_2 (commensurate with 5×5 hBN supercell), and all energies are measured with respect to the vacuum level. The *GW* band structures in (b) and (c) are obtained by interpolating 25 explicitly computed valence bands (24 conduction bands) on the 5×5 **k** mesh to 6 valence bands (15 conduction bands) on 100 uniformly sampled **k** points along the high-symmetry lines. The seemingly "discontinuous" bands seen in (b) and (c) are likely due to the perturbative nature of G_0W_0 and the specific energy window used in the interpolation.

Furthermore, we note that the dielectric screening of the hBN substrate enhances the degeneracy lifting of some of the bilayer MoS_2 bands in addition to that captured at the PBE level. Figure 3(a) shows the color-coded PBE band structure for the interface formed between bilayer MoS_2 and four-layer hBN. Comparing it with the *GW* band structure of freestanding bilayer MoS_2 in Fig. 3(b), one finds that some degeneracies of the bilayer MoS_2 bands are lifted by the crystal field effect of the hBN, such as the CBM at the Γ point. However, the degeneracy lifting captured by PBE is not as pronounced for other bands, such as the CBM at the *K* point, a few inner valence bands at the Γ point [around −4.5 eV in Fig. 3(a) and −6.5 eV in Fig. 3(b)], and many other near-degenerate cases in the Brillouin zone. In fact, at the PBE level of theory, for those near-degenerate bands, the degeneracy lifting due to the substrate is only on the order of 10^{-6} eV. Notably, the substrate dielectric screening greatly enhances the degeneracy lifting, causing a band splitting on the order of 10 meV, which can be seen in the embedding *GW* results in Fig. 3(c).

Comparing the bilayer MoS_2 band structure in its freestanding form and after it is adsorbed on hBN, one finds that the former features many degeneracies due to the symmetry of the two MoS_2 layers. The symmetry is broken, and the degeneracies are lifted when bilayer MoS_2 is adsorbed on substrates such as the four-layer hBN considered here. It is still an open question whether or not the approximate electronic structure methods in use (PBE and G_0W_0) can preserve certain symmetries that are protected and break others that should be broken in the interface. We find that the specific density functional used here, namely, the PBE, is able to lift some degeneracies when MoS_2 is adsorbed on hBN, capturing the orbital mixing between MoS_2 and hBN that is part of the crystal field effects. However, PBE seems to have difficulty with completely lifting the degeneracies in other bands and **k** points (causing only a band splitting of about 10^{-6} eV, as we discussed above). For those near-degenerate bands in PBE, the embedding *GW* approach is able to further break the symmetry and enhance the degeneracy lifting, causing a band splitting on the order of 10 meV. The latter is physically a result of the dielectric screening of the substrate because one layer is in closer contact with the substrate and feels stronger dielectric screening than the other.

D. Mixed WS_2/MoS_2 bilayer on four-layer hBN

In this section, we examine the dielectric effect of the hBN substrate on the electronic structure of the mixed WS_2/MoS_2 bilayer and show that different placements of the hBN lead to different modulations of the WS_2/MoS_2 bilayer band structure.

Figures 4(b) and 4(c) compare the *GW* band structure of the WS_2/MoS_2 bilayer in its freestanding phase and after it is adsorbed on the four-layer hBN substrate. In both panels, blue dots denote the *GW* band structure of the freestanding WS_2/MoS_2 bilayer (identical in the two panels), where we obtain 2.11 eV for the gap between Γ and *K* (compared to 1.96 eV in Ref. [69]) and 2.50 eV for the direct band gap at *K* (compared to 2.42 eV in Ref. [70]). In Fig. 4(b) [Fig. 4(c)], the red dots denote the band structure computed from dielectric embedding *GW*, taking into account the dielectric screening effects from the four-layer hBN that is placed close to the WS_2 (MoS_2) side, as shown in Fig. 1(d) [Fig. 1(c)]. We first note that the qualitative features of the WS_2/MoS_2 bands are preserved upon adsorption on hBN. The band gap in Fig. 4(b) is 1.93 eV, compared to 1.86 eV in Fig. 4(c). We note that this difference in the band gap is consistent with the trend in the dielectric function of the embedded WS_2/MoS_2 system: $\epsilon_{\mathbf{G}=0,\mathbf{G}'=0}(\mathbf{q})$ is slightly smaller for the case in Fig. 4(b) for every **q** point in the Brillouin zone (**G** and **G**′ are reciprocal-space lattice vectors). Physically, this can be attributed to the slightly smaller in-plane dielectric constant in WS_2 compared to MoS_2 [71].

Crucially, the valence band energies are renormalized by the substrate to a greater extent than the conduction band energies (compare red dots with blue dots) in Fig. 4(b), and the scenario is the opposite in Fig. 4(c). To understand

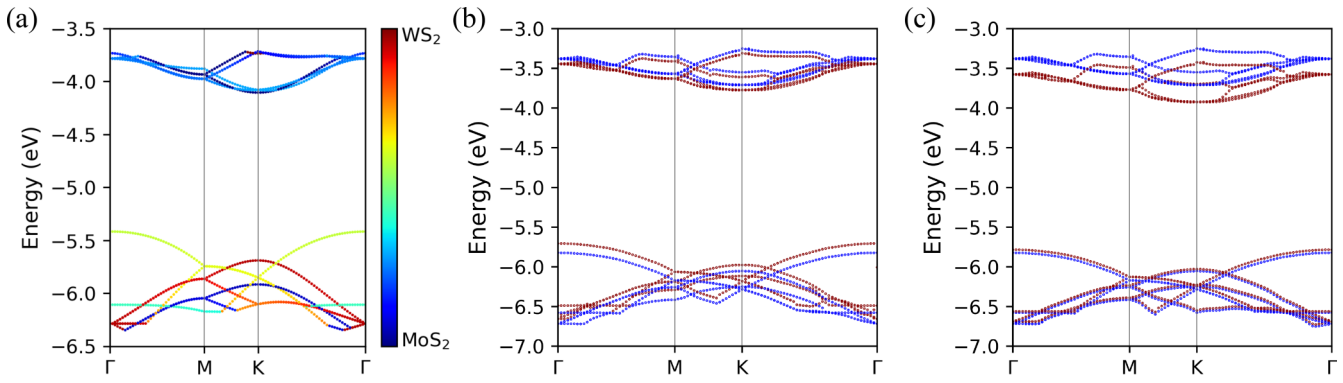

FIG. 4. (a) Color-coded PBE band structure of the freestanding WS_2/MoS_2 heterobilayer. In both (b) and (c), blue dots denote the *GW* band structure of the freestanding WS_2/MoS_2 heterobilayer, and red dots denote the band structure from dielectric embedding *GW* calculations of the WS_2/MoS_2 heterobilayer. In (b) [(c)], the WS_2 (MoS_2) side is closer to the four-layer hBN substrate, as shown in Fig. 1(d) [Fig. 1(c)]. All calculations are carried out in a 4×4 supercell of the WS_2/MoS_2 heterobilayer (commensurate with the 5×5 hBN supercell), and all energies are measured with respect to the vacuum level.

this phenomenon, we identify the nature of the valence and conduction bands of the freestanding WS_2/MoS_2 bilayer. In Fig. 4(a), we color-code the PBE band structure of the freestanding WS_2/MoS_2 bilayer, where the top valence band is localized on WS_2 and the bottom conduction band is localized on MoS_2. These orbital assignments are consistent with the literature [72]. When the mixed WS_2/MoS_2 bilayer is adsorbed on the hBN substrate with the WS_2 (MoS_2) side facing the substrate, the dielectric screening of the hBN has a higher impact on the valence (conduction) bands of the mixed WS_2/MoS_2 bilayer due to its spatial closeness to WS_2 (MoS_2). This spatially dependent dielectric screening is reflected in the band structure calculated from the dielectric embedding *GW*, i.e., the red dots in Figs. 4(b) and 4(c). In conclusion, adsorbate orbitals localized closer to the substrate experience stronger screening from the substrate, leading to larger energy renormalization than those localized farther away from the substrate.

We note that Ref. [11] reported different band onset energies for two vertical stacking configurations, MoS_2/WS_2/quartz and WS_2/MoS_2/quartz, based on scanning tunneling spectroscopy results. Although our work focuses on a different substrate, our results qualitatively explain the phenomenon observed in Ref. [11] in terms of the spatial dependence of the substrate dielectric screening. We further comment that the dielectric embedding *GW* approach is capable of capturing this effect efficiently. The placement of the substrate provides an effective way to selectively tune the band gaps of complex heterostructures.

IV. CONCLUSIONS

In this work, we have carried out dielectric embedding *GW* calculations to scrutinize the dielectric screening effects of the hBN substrate on the electronic structure of TMD adsorbates. We considered three sets of systems: (i) monolayer MoS_2 adsorbed on one-, two-, three-, and four-layer hBN; (ii) bilayer MoS_2 adsorbed on four-layer hBN; and (iii) a mixed WS_2/MoS_2 bilayer adsorbed on four-layer hBN with either WS_2 or MoS_2 facing the substrate. Our main findings are the following: (i) Monolayer hBN provides nearly negligible screening to the adsorbate, and the dielectric screening effect of the hBN substrate converges at four layers. (ii) A commonly used approximation, i.e., the neglect of the in-plane local-field components of the hBN polarizability χ^0_{hBN}, can introduce an error of about 0.2 eV in the gap of the TMD adsorbate. (iii) The dielectric effect of the substrate enhances the symmetry breaking of the bilayer MoS_2 in addition to the crystal field effect, and (iv) different placements of the substrate can be used to selectively modulate the valence or conduction bands of the mixed WS_2/MoS_2 bilayer. Additionally, we have found that the gap of the mixed WS_2/MoS_2 bilayer is slightly smaller when the MoS_2 side is placed closer to the substrate. Overall, the qualitative trends derived from our work provide insights into substrate-induced properties and substrate-based band structure engineering, and we hope our work provides a paradigm for future studies of interfaces with physisorption.

ACKNOWLEDGMENTS

We thank Prof. Li Yang for fruitful discussions. Z.-F.L. acknowledges NSF CAREER Award No. DMR-2044552. O.A. acknowledges a summer dissertation fellowship and a Rumble fellowship and the A. Paul and Carole C. Schaap endowed distinguished graduate award in chemistry at Wayne State University. DFT calculations used computational resources at the Center for Functional Nanomaterials (CFN), which is a U.S. Department of Energy Office of Science User Facility at Brookhaven National Laboratory under Contract No. DE-SC0012704. Large-scale *GW* calculations used resources at the National Energy Research Scientific Computing Center (NERSC), a U.S. Department of Energy Office of Science User Facility located at Lawrence Berkeley National Laboratory, operated under Contract No. DE-AC02-05CH11231 through NERSC Award No. BES-ERCAP0020328, as well as the Extreme Science and Engineering Discovery Environment (XSEDE), which is supported by NSF Grant No. ACI-1548562 through allocation PHY220043.

[1] A. Splendiani, L. Sun, Y. Zhang, T. Li, J. Kim, C.-Y. Chim, G. Galli, and F. Wang, Emerging photoluminescence in monolayer MoS_2, Nano Lett. **10**, 1271 (2010).

[2] M. Chhowalla, H. S. Shin, G. Eda, L.-J. Li, K. P. Loh, and H. Zhang, The chemistry of two-dimensional layered transition metal dichalcogenide nanosheets, Nat. Chem. **5**, 263 (2013).

[3] D. Jariwala, V. K. Sangwan, L. J. Lauhon, T. J. Marks, and M. C. Hersam, Emerging device applications for semiconducting two-dimensional transition metal dichalcogenides, ACS Nano **8**, 1102 (2014).

[4] D. Y. Qiu, F. H. da Jornada, and S. G. Louie, Screening and many-body effects in two-dimensional crystals: Monolayer MoS_2, Phys. Rev. B **93**, 235435 (2016).

[5] S. Wang, X. Wang, and J. H. Warner, All chemical vapor deposition growth of MoS_2:h-BN vertical van der Waals heterostructures, ACS Nano **9**, 5246 (2015).

[6] Q. Ji, Y. Zhang, Y. Zhang, and Z. Liu, Chemical vapour deposition of group-VIB metal dichalcogenide monolayers: Engineered substrates from amorphous to single crystalline, Chem. Soc. Rev. **44**, 2587 (2015).

[7] A. Sebastian, R. Pendurthi, T. H. Choudhury, J. M. Redwing, and S. Das, Benchmarking monolayer MoS_2 and WS_2 field-effect transistors, Nat. Commun. **12**, 693 (2021).

[8] W. Liu, J. Kang, D. Sarkar, Y. Khatami, D. Jena, and K. Banerjee, Role of metal contacts in designing high-performance monolayer n-type WSe_2 field effect transistors, Nano Lett. **13**, 1983 (2013).

[9] V. Podzorov, M. E. Gershenson, C. Kloc, R. Zeis, and E. Bucher, High-mobility field-effect transistors based on transition metal dichalcogenides, Appl. Phys. Lett. **84**, 3301 (2004).

[10] J. Ryou, Y.-S. Kim, K. C. Santosh, and K. Cho, Monolayer MoS_2 bandgap modulation by dielectric environments and tunable bandgap transistors, Sci. Rep. **6**, 29184 (2016).

[11] H. M. Hill, A. F. Rigosi, K. T. Rim, G. W. Flynn, and T. F. Heinz, Band alignment in MoS_2/WS_2 transition metal dichalcogenide heterostructures probed by scanning tunneling microscopy and spectroscopy, Nano Lett. **16**, 4831 (2016).

[12] D. Y. Qiu, F. H. da Jornada, and S. G. Louie, Environmental screening effects in 2D materials: Renormalization of the bandgap, electronic structure, and optical spectra of few-layer black phosphorus, Nano Lett. **17**, 4706 (2017).

[13] A. Raja, A. Chaves, J. Yu, G. Arefe, H. M. Hill, A. F. Rigosi, T. C. Berkelbach, P. Nagler, C. Schüller, T. Korn, C. Nuckolls, J. Hone, L. E. Brus, T. F. Heinz, D. R. Reichman, and A. Chernikov, Coulomb engineering of the bandgap and excitons in two-dimensional materials, Nat. Commun. **8**, 15251 (2017).

[14] Y. J. Zheng, Y. L. Huang, Y. Chen, W. Zhao, G. Eda, C. D. Spataru, W. Zhang, Y.-H. Chang, L.-J. Li, D. Chi, S. Y. Quek, and A. T. S. Wee, Heterointerface screening effects between organic monolayers and monolayer transition metal dichalcogenides, ACS Nano **10**, 2476 (2016).

[15] Y. Cho and T. C. Berkelbach, Environmentally sensitive theory of electronic and optical transitions in atomically thin semiconductors, Phys. Rev. B **97**, 041409(R) (2018).

[16] N. Zibouche, M. Schlipf, and F. Giustino, GW band structure of monolayer MoS_2 using the SternheimerGW method and effect of dielectric environment, Phys. Rev. B **103**, 125401 (2021).

[17] C. Lattyak, K. Gehrke, and M. Vehse, Layer-thickness-dependent work function of MoS_2 on metal and metal oxide substrates, J. Phys. Chem. C **126**, 13929 (2022).

[18] S. E. Panasci, E. Schilirò, G. Greco, M. Cannas, F. M. Gelardi, S. Agnello, F. Roccaforte, and F. Giannazzo, Strain, doping, and electronic transport of large area monolayer MoS_2 exfoliated on gold and transferred to an insulating substrate, ACS Appl. Mater. Interfaces **13**, 31248 (2021).

[19] S. G. Sørensen, H. G. Füchtbauer, A. K. Tuxen, A. S. Walton, and J. V. Lauritsen, Structure and electronic properties of in situ synthesized single-layer MoS_2 on a gold surface, ACS Nano **8**, 6788 (2014).

[20] X. Liu, I. Balla, H. Bergeron, G. P. Campbell, M. J. Bedzyk, and M. C. Hersam, Rotationally commensurate growth of MoS_2 on epitaxial graphene, ACS Nano **10**, 1067 (2016).

[21] Y. L. Huang, Y. Chen, W. Zhang, S. Y. Quek, C.-H. Chen, L.-J. Li, W.-T. Hsu, W.-H. Chang, Y. J. Zheng, W. Chen, and A. T. S. Wee, Bandgap tunability at single-layer molybdenum disulphide grain boundaries, Nat. Commun. **6**, 6298 (2015).

[22] M.-H. Chiu, C. Zhang, H.-W. Shiu, C.-P. Chuu, C.-H. Chen, C.-Y. S. Chang, C.-H. Chen, M.-Y. Chou, C.-K. Shih, and L.-J. Li, Determination of band alignment in the single-layer MoS_2/WSe_2 heterojunction, Nat. Commun. **6**, 7666 (2015).

[23] C. Zhang, A. Johnson, C.-L. Hsu, L.-J. Li, and C.-K. Shih, Direct imaging of band profile in single layer MoS_2 on graphite: Quasiparticle energy gap, metallic edge states, and edge band bending, Nano Lett. **14**, 2443 (2014).

[24] H. Li, J. Wu, Z. Yin, and H. Zhang, Preparation and applications of mechanically exfoliated single-layer and multi layer MoS_2 and WSe_2 nanosheets, Acc. Chem. Res. **47**, 1067 (2014).

[25] C.-P. Lu, G. Li, J. Mao, L.-M. Wang, and E. Y. Andrei, Bandgap, mid-gap states, and gating effects in MoS_2, Nano Lett. **14**, 4628 (2014).

[26] P. K. Chow, E. Singh, B. C. Viana, J. Gao, J. Luo, J. Li, Z. Lin, A. L. Elias, Y. Shi, Z. Wang, M. Terrones, and N. Koratkar, Wetting of mono and few-layered WS_2 and MoS_2 films supported on Si/SiO_2 substrates, ACS Nano **9**, 3023 (2015).

[27] X. Han, J. Lin, J. Liu, N. Wang, and D. Pan, Effects of hexagonal boron nitride encapsulation on the electronic structure of few-layer MoS_2, J. Phys. Chem. C **123**, 14797 (2019).

[28] X. Zhang, F. Zhang, Y. Wang, D. S. Schulman, T. Zhang, A. Bansal, N. Alem, S. Das, V. H. Crespi, and M. Terrones, Defect-controlled nucleation and orientation of WSe_2 on hBN: A route to single-crystal epitaxial monolayers, ACS Nano **13**, 3341 (2019).

[29] D. R. Penn, Wave-number-dependent dielectric function of semiconductors, Phys. Rev. **128**, 2093 (1962).

[30] J. Klein, A. Kerelsky, M. Lorke, M. Florian, F. Sigger, J. Kiemle, M. C. Reuter, T. Taniguchi, K. Watanabe, J. J. Finley, A. N. Pasupathy, A. W. Holleitner, F. M. Ross, and U. Wurstbauer, Impact of substrate induced band tail states on the electronic and optical properties of MoS_2, Appl. Phys. Lett. **115**, 261603 (2019).

[31] S. Kümmel and L. Kronik, Orbital-dependent density functionals: Theory and applications, Rev. Mod. Phys. **80**, 3 (2008).

[32] J. P. Perdew and M. Levy, Physical Content of the Exact Kohn-Sham Orbital Energies: Band Gaps and Derivative Discontinuities, Phys. Rev. Lett. **51**, 1884 (1983).

[33] W. Yang, A. J. Cohen, and P. Mori-Sánchez, Derivative discontinuity, bandgap and lowest unoccupied molecular orbital in density functional theory, J. Chem. Phys. **136**, 204111 (2012).

[34] L. Hedin, New method for calculating the one-particle Green's function with application to the electron-gas problem, Phys. Rev. **139**, A796 (1965).

[35] G. Strinati, H. J. Mattausch, and W. Hanke, Dynamical aspects of correlation corrections in a covalent crystal, Phys. Rev. B **25**, 2867 (1982).

[36] M. S. Hybertsen and S. G. Louie, Electron correlation in semiconductors and insulators: Band gaps and quasiparticle energies, Phys. Rev. B **34**, 5390 (1986).

[37] M. Rohlfing and S. G. Louie, Electron-hole excitations and optical spectra from first principles, Phys. Rev. B **62**, 4927 (2000).

[38] H. Shi, H. Pan, Y.-W. Zhang, and B. I. Yakobson, Quasiparticle band structures and optical properties of strained monolayer MoS_2 and WS_2, Phys. Rev. B **87**, 155304 (2013).

[39] D. Y. Qiu, F. H. da Jornada, and S. G. Louie, Optical spectrum of MoS_2: Many-Body Effects and Diversity of Exciton States, Phys. Rev. Lett. **111**, 216805 (2013).

[40] A. Ramasubramaniam, Large excitonic effects in monolayers of molybdenum and tungsten dichalcogenides, Phys. Rev. B **86**, 115409 (2012).

[41] T. Cheiwchanchamnangij and W. R. L. Lambrecht, Quasiparticle band structure calculation of monolayer, bilayer, and bulk MoS_2, Phys. Rev. B **85**, 205302 (2012).

[42] M. M. Ugeda, A. J. Bradley, S.-F. Shi, F. H. da Jornada, Y. Zhang, D. Y. Qiu, W. Ruan, S.-K. Mo, Z. Hussain, Z.-X. Shen, F. Wang, S. G. Louie, and M. F. Crommie, Giant bandgap renormalization and excitonic effects in a monolayer transition metal dichalcogenide semiconductor, Nat. Mater. **13**, 1091 (2014).

[43] J. B. Neaton, M. S. Hybertsen, and S. G. Louie, Renormalization of Molecular Electronic Levels at Metal-Molecule Interfaces, Phys. Rev. Lett. **97**, 216405 (2006).

[44] K. S. Thygesen and A. Rubio, Renormalization of Molecular Quasiparticle Levels at Metal-Molecule Interfaces: Trends across Binding Regimes, Phys. Rev. Lett. **102**, 046802 (2009).

[45] Z.-F. Liu, F. H. da Jornada, S. G. Louie, and J. B. Neaton, Accelerating GW-based energy level alignment calculations for molecule-metal interfaces using a substrate screening approach, J. Chem. Theory Comput. **15**, 4218 (2019).

[46] F. Xuan, Y. Chen, and S. Y. Quek, Quasiparticle levels at large interface systems from many-body perturbation theory: The XAF-GW method, J. Chem. Theory Comput. **15**, 3824 (2019).

[47] J. Frimpong and Z.-F. Liu, Quasiparticle electronic structure of two-dimensional heterotriangulene-based covalent organic frameworks adsorbed on Au(111), J. Phys.: Condens. Matter **33**, 254004 (2021).

[48] M. Drüppel, T. Deilmann, P. Krüger, and M. Rohlfing, Diversity of trion states and substrate effects in the optical properties of an MoS_2 monolayer, Nat. Commun. **8**, 2117 (2017).

[49] Z.-F. Liu, Dielectric embedding GW for weakly coupled molecule-metal interfaces, J. Chem. Phys. **152**, 054103 (2020).

[50] O. Adeniran and Z.-F. Liu, Quasiparticle electronic structure of phthalocyanine:TMD interfaces from first-principles GW, J. Chem. Phys. **155**, 214702 (2021).

[51] K. Berland and P. Hyldgaard, Exchange functional that tests the robustness of the plasmon description of the van der Waals density functional, Phys. Rev. B **89**, 035412 (2014).

[52] R. S. Pease, An x-ray study of boron nitride, Acta Crystallogr. **5**, 356 (1952).

[53] D. Wickramaratne, L. Weston, and C. G. Van de Walle, Monolayer to bulk properties of hexagonal boron nitride, J. Phys. Chem. C **122**, 25524 (2018).

[54] M. Schlipf and F. Gygi, Optimization algorithm for the generation of ONCV pseudopotentials, Comput. Phys. Commun. **196**, 36 (2015).

[55] D. R. Hamann, Optimized norm-conserving Vanderbilt pseudopotentials, Phys. Rev. B **88**, 085117 (2013).

[56] P. Giannozzi *et al.*, Advanced capabilities for materials modelling with Quantum ESPRESSO, J. Phys.: Condens. Matter **29**, 465901 (2017).

[57] K. Momma and F. Izumi, VESTA: A three-dimensional visualization system for electronic and structural analysis, J. Appl. Crystallogr. **41**, 653 (2008).

[58] J. Deslippe, G. Samsonidze, D. A. Strubbe, M. Jain, M. L. Cohen, and S. G. Louie, BerkeleyGW: A massively parallel computer package for the calculation of the quasiparticle and optical properties of materials and nanostructures, Comput. Phys. Commun. **183**, 1269 (2012).

[59] J. P. Perdew, K. Burke, and M. Ernzerhof, Generalized Gradient Approximation Made Simple, Phys. Rev. Lett. **77**, 3865 (1996).

[60] S. Ismail-Beigi, Truncation of periodic image interactions for confined systems, Phys. Rev. B **73**, 233103 (2006).

[61] J. Deslippe, G. Samsonidze, M. Jain, M. L. Cohen, and S. G. Louie, Coulomb-hole summations and energies for *GW* calculations with limited number of empty orbitals: A modified static remainder approach, Phys. Rev. B **87**, 165124 (2013).

[62] M. L. Trolle, T. G. Pedersen, and V. Véniard, Model dielectric function for 2D semiconductors including substrate screening, Sci. Rep. **7**, 39844 (2017).

[63] C. Brülke, O. Bauer, and M. M. Sokolowski, The influence of an interfacial hBN layer on the fluorescence of an organic molecule, Beilstein J. Nanotechnol. **11**, 1663 (2020).

[64] K. F. Mak, C. Lee, J. Hone, J. Shan, and T. F. Heinz, Atomically Thin MoS_2: A New Direct-Gap Semiconductor, Phys. Rev. Lett. **105**, 136805 (2010).

[65] D. J. Rizzo, Q. Dai, C. Bronner, G. Veber, B. J. Smith, M. Matsumoto, S. Thomas, G. D. Nguyen, P. R. Forrester, W. Zhao, J. H. Jørgensen, W. R. Dichtel, F. R. Fischer, H. Li, J.-L. Bredas, and M. F. Crommie, Revealing the local electronic structure of a single-layer covalent organic framework through electronic decoupling, Nano Lett. **20**, 963 (2020).

[66] M. I. B. Utama, H. Kleemann, W. Zhao, C. S. Ong, F. H. da Jornada, D. Y. Qiu, H. Cai, H. Li, R. Kou, S. Zhao, S. Wang, K. Watanabe, T. Taniguchi, S. Tongay, A. Zettl, S. G. Louie, and F. Wang, A dielectric-defined lateral heterojunction in a monolayer semiconductor, Nat. Electron. **2**, 60 (2019).

[67] M. Rohlfing, Electronic excitations from a perturbative LDA+*GdW* approach, Phys. Rev. B **82**, 205127 (2010).

[68] M. H. Naik and M. Jain, Substrate screening effects on the quasiparticle band gap and defect charge transition levels in MoS_2, Phys. Rev. Mater. **2**, 084002 (2018).

[69] L. Debbichi, O. Eriksson, and S. Lebègue, Electronic structure of two-dimensional transition metal dichalcogenide bilayers from *ab initio* theory, Phys. Rev. B **89**, 205311 (2014).

[70] S. Gao, L. Yang, and C. D. Spataru, Interlayer coupling and gate-tunable excitons in transition metal dichalcogenide heterostructures, Nano Lett. **17**, 7809 (2017).

[71] A. Laturia, M. L. Van de Put, and W. G. Vandenberghe, Dielectric properties of hexagonal boron nitride and transition metal dichalcogenides: From monolayer to bulk, npj 2D Mater. Appl. **2**, 6 (2018).

[72] M. Bernardi, M. Palummo, and J. C. Grossman, Extraordinary sunlight absorption and one nanometer thick photovoltaics using two-dimensional monolayer materials, Nano Lett. **13**, 3664 (2013).